Spatial-temporal and modal analysis of propeller induced ground vortices by particle image velocimetry

Yang, Yang; Sciacchitano, Andrea; Veldhuis, Leo; Eitelberg, Georg

DOI
10.1063/1.4964685

Publication date
2016

Document Version
Accepted author manuscript

Published in
Physics of Fluids

Spatial-temporal and modal analysis of propeller induced ground vortices by Particle Image Velocimetry

Y. Yang, A. Sciacchitano, L. L. M. Veldhuis, and G. Eitelberg

TU Delft, Delft, Netherlands, 2629HS

email: Y.Yang-1@tudelft.nl

Abstract

During the ground operation of aircraft, there is potentially a system of vortices generated from the ground toward the propulsor, commonly denoted as ground vortices. Although extensive research has been conducted on ground vortices induced by turbofans which were simplified by suction tubes, these studies cannot well capture the properties of ground vortices induced by propellers, e.g. the flow phenomena due to intermittent characteristics of blade passing and the presence of slipstream of the propeller. Therefore, the investigation of ground vortices induced by a propeller is performed to improve understanding to these phenomena. The distributions of velocities in two different planes containing the vortices were measured by high frequency Particle Image Velocimetry (PIV). These planes are a wall-parallel plane in close proximity to the ground and a wall-normal plane upstream of the propeller. The instantaneous flow fields feature highly unsteady flow in both of these two planes. The spectral analysis is conducted in these two flow fields and the energetic frequencies are quantified. The flow fields are further evaluated by applying the Proper Orthogonal Decomposition (POD) analysis to capture the coherent flow structures. Consistent flow structures with strong contributions to the turbulent kinetic energy are noticed in the two planes.

1. Introduction

The generation of ground vortices is a phenomenon that occurs during aircraft ground operations. This phenomenon consists of a system of vortices formed on the ground that ascend into the aircraft engine, thus causing unsteady and non-uniform inflow effects. Ground vortices can be observed during aircraft taxiing and engine maintenance when rain droplets are present or air condensation occurs in the vortex region. One example of such vortical flow occurs on an aircraft propeller is shown in Fig. 1. The ground vortices were first investigated because of the concern of foreign object damage (FOD) to the engine [1]. It is reported that 40% of engine repairs is due to the foreign object damage when the aircraft is operated near the ground [2].

Extensive research on the detail of the ground vortices has been conducted on the simplified turbofan model by a suction tube [3, 4, 5, 6]. These investigations have greatly improved the understanding on the mechanism of the formation of the ground vortices. For the headwind condition, which is the situation of our investigation, ground vortices are generated by the suction of vorticity (wall-parallel components) existed near the ground into wall-normal component [3]. These vortex near the ground are ascribed to the far field boundary layer [3, 7, 8]; moreover, these vorticity could also be generated by the pressure gradient on the ground induced by the propeller suction according to the vorticity generation equation [9]. For the take-off condition, the wall-parallel components of vorticity are generated by the pressure gradient on the ground solely. For the crosswind condition, vortex shedding from the shroud of the engine was proposed to be the ground vortex origin [3]. The unsteadiness of ground vortices when the suction tube is operated at headwind and crosswind conditions are studied in [10] and [5] respectively. The results show that vortex meandering and velocity fluctuation feature peak values at Strouhal number (based on the inlet velocity and inlet diameter) of order of $O(10^{-3})\sim O(10^{-2})$.

The vortices formed near the ground are convected to the engine due to the engine suction. The entry positions of the vortices are mostly at the bottom of the intake [4, 5, 11]. This flow asymmetry causes the ground vortices to affect the distortion of the engine inflow [12]. The total pressure distortion was shown to increase monotonically with the thrust coefficient when the wind tunnel wall was

synchronized with the free stream velocity (the wind tunnel wall was replaced by a moving belt) to eliminate the boundary layer on the ground.

Fig. 1 Occurrence of ground vortex on the outboard propeller of aircraft C130 [13] (This figure is taken from NASA SP-514 [J. F., Campbell, and J. R., Patterns in the sky-natural visualization of aircraft flow fields] and used with permission of NASA).

It is found that the majority of research about ground vortices is conducted on the turbofan model, and there is no open literature found for ground vortices induced by propellers. For an un-shrouded rotor (propeller), the flow field due to the interaction between the ground and rotor (together with its slipstream) may feature different characteristics from the shrouded turbofans. For the above reason, the ground vortices generated by a propeller are studied experimentally in this paper, in terms of the flow topology, unsteadiness, and coherent fluctuating flow structures in the discrete planes containing the ground vortices.

2. Experimental setup

2.1.Wind tunnel and propeller rigs

The tests were carried out in a low-speed, closed-loop open-jet wind tunnel in Delft University of Technology. The tunnel has an octagonal test section and a maximum speed of 35 m/s. The inflow velocity was set at a relatively low speed, of $U_\infty = 2.7\ m/s$, to achieve high thrust coefficients needed to generate ground vortices. The turbulence intensity of the free stream at this velocity is 0.5%, as shown in Appendix A.

In order to simulate a propeller engine operating near the ground, an isolated 8-bladed model of the propeller was mounted over a flat table, as shown in Fig. 2. The propeller support is adjustable to allow change in the elevation above the ground table, and the height of the propeller is fixed at $h = 1.46\ R$ in this paper, where R = 0.152 m is the radius of the propeller. The ground table has a transparent window so cameras can look through it. The total length of the propeller model is L = 0.904 m, involving spinner, hub and nacelle.

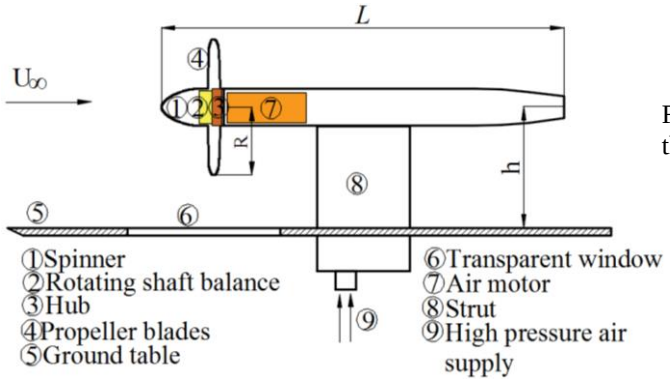

Fig. 2 Schematic overview of the experimental arrangement.

The propeller was directly coupled to a rotating shaft balance (RSB) that measured the thrust and torque produced by the propeller. The propeller was driven by a TDI 1999 pneumatic motor, which has a maximum RPM of 22,500. The RSB data acquisition frequency was 50 kHz; data was averaged over 5 seconds to obtain the mean thrust and torque values. The propeller was operated at a high thrust coefficient of $T_c = 27.3$ to generate ground vortices ($T_c = T/(\rho {U_\infty}^2 D^2)$, where T is the thrust

generated by the propeller, ρ is the air density, D is the diameter of the propeller). An even higher thrust coefficient $T_c = 48.2$ is also performed to compare the flow fields with that measured at $T_c = 27.3$.

2.2.PIV set up

Stereo PIV measurements are conducted at the planes involving ground vortices. The flow was seeded with micron-sized water-glycol particles produced by a SAFEX Twin Fog Double Power smoke generator inserted in the settling chamber. The Quantronix Darwin Duo Nd-YLF double pulse laser was used for illumination. The particle images are recorded by Photron FastCAM SA1.1 CMOS cameras (1024 × 1024 pixels at 5400 fps,12 bits, 20 μm pixel pitch).

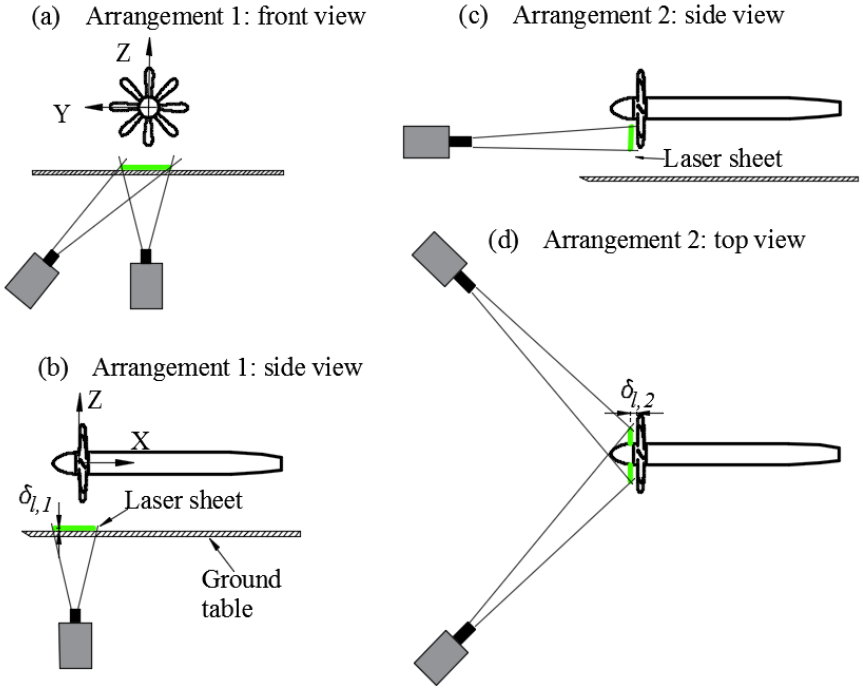

Fig. 3 Setups of high frequency PIV measurements. (a) and (b): arrangement 1 for the measurement in the wall parallel plane; (c) and (d): arrangement 2 for the measurement in the wall normal plane.

The setup of high frequency stereoscopic-PIV measurements conducted at the wall parallel plane (arrangement 1) is shown in Fig. 3 (a) and (b). The distance of the field of view is 7mm above the ground, $(\mathrm{Z} - Z_{wall})/\mathrm{R} = 0.046 \approx 0.1\delta_{BL}$, δ_{BL} is the boundary layer thickness as shown in Appendix A. The imaging system is based on a 35 mm Nikkor objective set at $f\# = 4$ and a 50 mm Nikkor objective set at $f_{\#} = 4$. The magnification factor is 0.14. The measurement was conducted at frequency of 1500HZ for a trail, and then it is found that the flow features low frequency characteristics. Therefore， the measurements at this plane were conducted at a relatively low frequency of 500HZ and sequences of 1500 images pairs were acquired.

Stereoscopic-PIV tests were also carried out at the wall normal plane upstream of the propeller at $X/R = -0.16$ (arrangement 2). The forward and backward scattering cameras are based on 200 mm Nikkor objectives set at $f_{\#} = 11$ and $f_{\#} = 8$ respectively. The magnification factor is 0.15. The flow field in this plane is dominated by the blade bypassing induced flow and features high frequency. Therefore， the measurements at this plane were conducted at frequency of 1500HZ (propeller rotation is 58HZ, and the blade passing frequency is 464 HZ) and sequences of 2500 images pairs were acquired.

2.3.Uncertainty analysis

The uncertainty of PIV data is estimated by the image matching method [14]. The image matching method uses the measured velocity field to match the particle images of the recordings based on the processing algorithm (for example by window deformation or window shift). The approach detects particle images in each interrogation window. In case of exact velocity measurements, the particle images of the two recordings would match perfectly. In real experiments, the paired particle images do not match exactly and feature a positional disparity between them. The positional disparity is

computed as the distance between the centroids of the particle images. The measurement uncertainty is determined within each interrogation window from the mean value and the statistical dispersion of the positional disparity vector.

In the wall parallel plane, the uncertainty of the instantaneous velocity fields at 95% confidence level is 0.02 m/s. For the wall normal plane PIV measurement, the uncertainty is 0.18 m/s for the in-plane velocity components and 0.17 m/s for the out-of-plane velocity component. The uncertainty of the time averaged flow field is 0.01 m/s.

3. Analysis methods

3.1.Proper orthogonal decomposition

The inspection of flow structures in complex flows requires detecting and distinguishing them from the less coherent fluctuations. Proper Orthogonal Decomposition (POD) identifies basis functions (i.e. modes) that capture the average energy content from experimental or numerical data [15]. The "method of snapshots" as discussed in [16] is applied in this paper. The introduction of this method in our paper is focused on its application form.

The results of unsteady PIV measurement are a set of instantaneous velocities, i.e. three components of velocities ($\vec{U} = [U_X, U_Y, U_Z]$) in a 2D domain $\vec{X} = [X, Y]$ in our case. The fluctuation of the velocities defined in Reynolds decomposition is

$$\vec{U}(\vec{X}, t) = \bar{U}(\vec{X}, t) + \vec{u}(\vec{X}, t) \tag{3.1}$$

$\vec{U}(\vec{X}, t)$ is the instantaneous flow field, $\bar{U}(\vec{X})$ is the time averaged flow field; and $\vec{u}(\vec{X}, t)$ is the fluctuation part of the velocities.

The proper decomposition is then applied on the autocorrelation matrix C as reported in [17]. The matrix C is defined by

$$C_{i,j} = \frac{1}{N_s} \iint \vec{u}(\vec{X}, t_i)\vec{u}(\vec{X}, t_j)\, d\vec{X}. \tag{3.2}$$

N_s is the number of snapshots; the integral in our case is a summation for the discrete points of data. The size of C is determined by the number of snapshots and its dimension is $N_s \times N_s$.

The eigenvalues λ_n and the eigenvectors $A_n(\vec{X})$ of autocorrelation matrix satisfy

$$\mathrm{C}A_n(\vec{X}) = \lambda_n A_n(\vec{X}). \tag{3.3}$$

The POD mode is determined by

$$\overrightarrow{\phi_n}(\vec{X}) = \sum_{m=1}^{m=N_s} \vec{u}(\vec{X}, t_m) A_{m,n}(\vec{X}). \tag{3.4}$$

Furthermore, the measurement data contain temporal information that can be retrieved by projecting each snapshot onto the basis functions:

$$c_n(t) = \iint \vec{u}(\vec{X}, t)\overrightarrow{\phi_n}(\vec{X})\, d\vec{X} \tag{3.5}$$

The coefficient c_n indicates the correlation between the nth basis POD spatial mode and the instantaneous flow field [15, 16].

4. Results and analysis

4.1.Time resolved analysis of flow fields

Flow fields near the ground

The dynamic evolution of the flow fields captured in the wall parallel plane is shown in Fig. 4. The Z-component of the vorticity is normalized by the parameter of propeller diameter and the equivalent inflow velocity of the propeller and defined by $U_{eq} = U_\infty \sqrt{1 + 8 \cdot T_c/\pi}$.

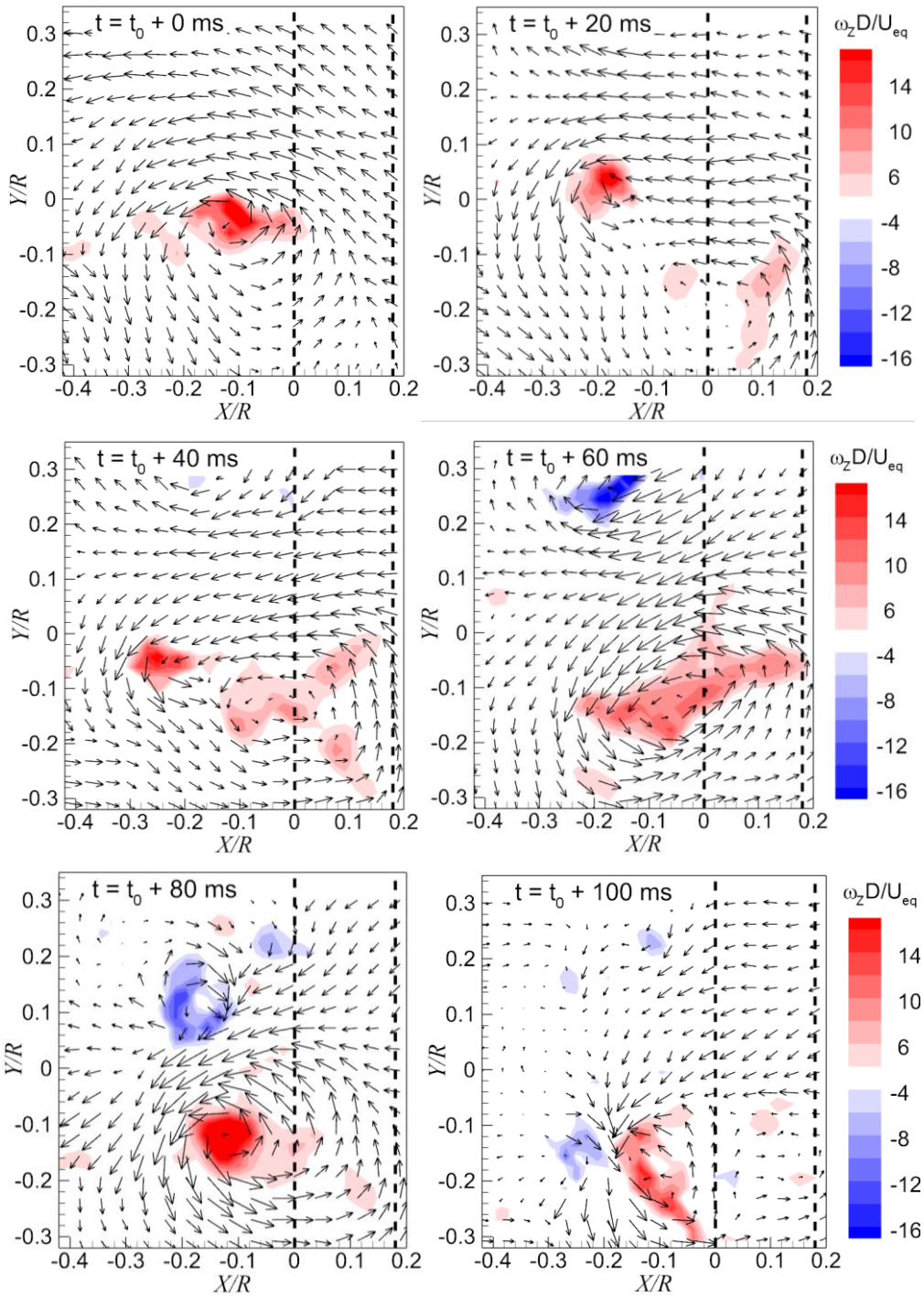

Fig. 4 Sequence of instantaneous flow fields in the horizontal plane above the ground. Superimposed are the color-coded magnitudes of non-dimensional wall-perpendicular vorticity. T_c= 27.3. The dashed line indicates the propeller projection.

Let us consider the instantaneous flow fields starting from $t = t_0$, as shown in the top left of Fig. 4. There is one dominant vortex with positive Z-component vorticity (counter-clockwise rotation direction), which is located upstream of the propeller. In the successive time, i.e. $t = t_0 + 20\,ms$, this vortex with positive Z-component vorticity remains and another region with distributed positive Z-component vorticity occurs at the bottom-right corner of the figure. They interact with each other and finally form a big vortex at time $t = t_0 + 60\,ms$. At the same time, it is also noticed that there is one region with negative vorticity located in the upper side of the figure. This vortex moves to the centre of the flow field at $t = t_0 + 80\,ms$. As the clockwise vortex (negative Z-component vorticity) becomes close to the counter-clockwise vortex, they are both weakened and move toward the bottom of the figure due to induced velocities by each other. The total duration of 100 ms for the time window was chosen, because of the empirical evidence that all characteristic formations in

our experiments occurred within this time widow at least once. No theoretical characteristic time for vortex formation was calculated.

As noticed in Fig. 4, the number of vortices observed in these instantaneous flow fields is not constant, e.g. one dominant vortex and two dominant vortices are observed. However, there is only one dominant vortex as shown in Fig. 1. This difference is mainly ascribed to two possible reasons. Firstly, the wind condition of the case as shown in Fig. 1 might be different from our tests (the wind condition in Fig. 1 is not mentioned in [13]). If there is a crosswind for the case as shown in Fig. 1, a single vortex is generated from the ground and this is extensively reported by others [5, 6]. Our case is tested at the headwind condition, so this could cause a difference. Secondly, even if the wind condition in Fig. 1 is the headwind condition, the unsteadiness of ground vortices would feature different number of vortices at different instants. As shown in Fig. 4, the number of vortices is not a constant. Sometime one single dominant vortex is observed, which is the same phenomenon as that shown in Fig. 1. Sometime two dominant vortices are observed, which is not shown in Fig. 1, but it does not necessarily mean it does not occur.

The out of plane component of the velocity at time $t = t_0$ is plotted in Fig. 5, which features regions with distributed negative and positive values of U_Z. It is noted that the axial velocity in the vortex centre near the ground is not the same as that of the wing tip vortex, which has a deficit or jet-like distribution of the axial velocity. This distribution is ascribed to the roll-up process of the wall parallel vortices, which have complex induced velocity in the out of plane component.

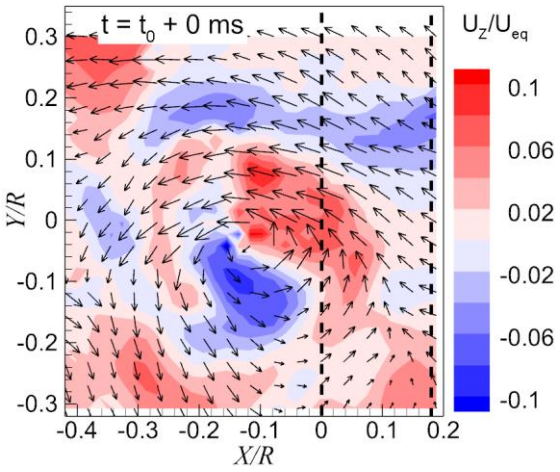

Fig. 5 The instantaneous flow field at time $t = t_0$ which is colour contoured by the out-of-plane component of the velocity. T_c= 27.3.

Flow fields directly upstream of the propeller

The dynamic evolution of the flow field in the plane upstream of the propeller, where the vortices go through before entering the propeller disk plane, is shown in Fig. 6.

The instantaneous flow field at time $t = t_1$ is shown in the top left of Fig. 6. One vortex with positive X-component vorticity is observed, as well as distributed negative X-component vorticity in the flow field. These distributed negative X-component vorticity concentrates and forms another dominant vortex at time $t = t_1 + 10\ ms$. At the subsequent time, i.e. $t = t_1 + 20\ ms$, the set of vortices move toward the right hand side of the propeller disk plane. At the time $t = t_1 + 30\ ms$, the dominant vortices in the field of view of the PIV measurement nearly disappear. Here, it appears sufficient to visualize the 30 ms time window to obtain all the characteristic features at least once.

In addition, the flow field colour contoured by the axial velocity at time $t = t_1$ is shown in Fig. 7. Still, the axial component of the velocity inside the vortex is overwhelmed by the induced velocity of the propeller; there is no excess velocity or deficit in the vortex core region observed.

The instantaneous flow fields selected for analysis both in the wall-parallel plane and the wall-normal plane capture the main characteristics of the flow field: the sign of the dominant vortex in the flow field varies in time; the vortices meandering in the measurement plane; the number of dominant vortices is not constant. The flow fields in other instants both in the wall parallel and the wall normal plane are in the video for the supplementary material.

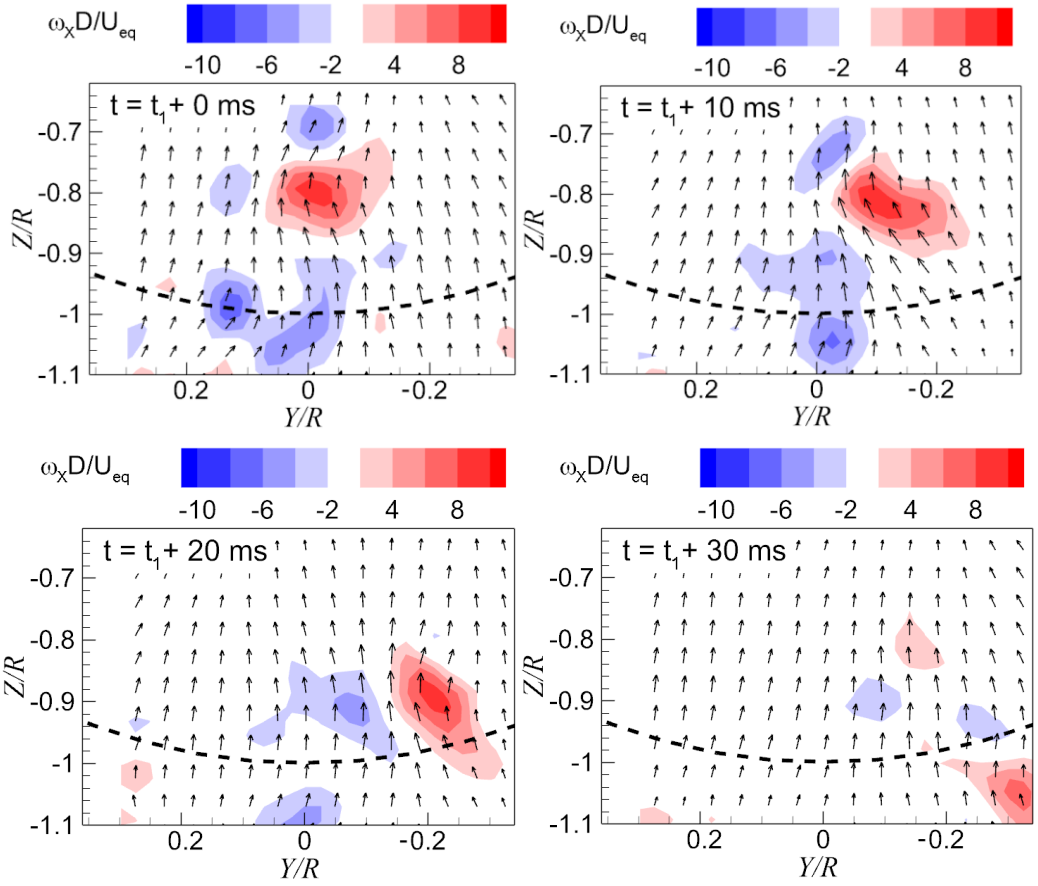

Fig. 6 Sequence of instantaneous flow fields in the plane upstream the propeller. Superimposed are the color-coded magnitudes of non-dimensional X-component vorticity. T_c= 27.3. The dashed line indicates the propeller projection.

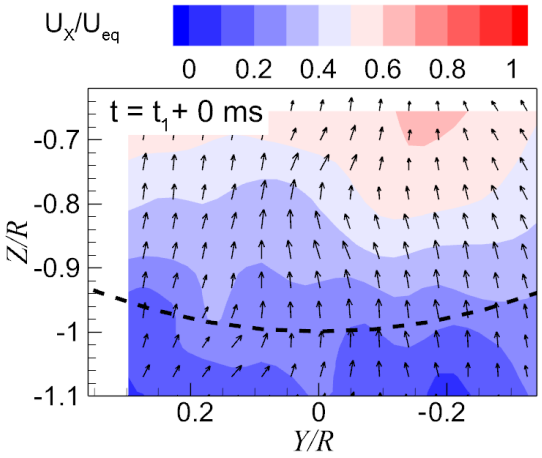

Fig. 7 The instantaneous flow field at time $t = t_1$ which is colour contoured by the out-of-plane component of the velocity.

Unsteadiness of ground vortices

The time resolved data is also utilized to analyse the energetic frequencies involved in the unsteadiness of ground vortices by means of spectral analysis. In this case, the power spectral analysis is performed on the Z-component vorticity in the wall-parallel plane (PIV arrangement 1). The Z-component vorticity is evaluated at three typical regions where ground vortices occur, i.e. $[X/R,\ Y/R] = [-0.1, 0.0], [-0.1, 0.2], [-0.1, -0.2]$ (Fig. 8). The Z-component of the vorticity is calculated by the mean value of a spatial kernel of 3×3 points to decrease the error propagated from each point. The parameter defined to normalize the frequency f of the vorticity fluctuation is fD/U_{eq}, which follows the same definition of the dimensionless frequency of the meandering of ground vortices induced by suction tubes as reported in [5, 10]. It should be mentioned that the

height of the propeller from the ground is not utilized to normalize the frequency, because the unsteadiness of ground vortices is assumed to be attributed to the turbulence in the boundary layer of the ground and the free stream. This assumption is made by considering the analogy between ground vortices and wing tip vortex, which are both shed from solid surfaces. The unsteadiness of a wing tip vortex is found to be due to the fluctuation of the free stream and the turbulence in the boundary layer of the wing [18]. Therefore, the height of the propeller above the ground is not a key parameter for the unsteadiness of ground vortices. In addition, the unsteadiness of the free stream and the boundary layer of the ground is quantified and reported in Appendix A, but not included for this normalization.

The dominant peaks are observed at the frequency range of $fD/U_{eq} = O(10^{-2})\sim O(10^{-1})$ for all the locations analysed, e.g. a dominant peak at frequency of $fD/U_{eq} = 0.017$ is observed at the position of $[X/R,\ Y/R] = [-0.1, 0.0]$. It is also noticed that the frequency content at different locations are different, which implies that the unsteadiness of ground vortices is not only dependent on the movement of the vortices, but also has impacts from other factors, e.g., the turbulence in the boundary layer, and the interaction between vortices. This frequency range of the ground vortices induced by the propeller is consistent with that observed in [10] for the ground vortices induced by a suction tube model. This consistence implies that the unsteadiness of ground vortices near the ground is independent of the intermittent flow induced by the blade passing. This is further confirmed by evaluating the power spectral near the blade passing frequency of $fD/U_{eq} = 6.598$ during a trial test in our measurements, and no pulse is found near this frequency so it is not shown here.

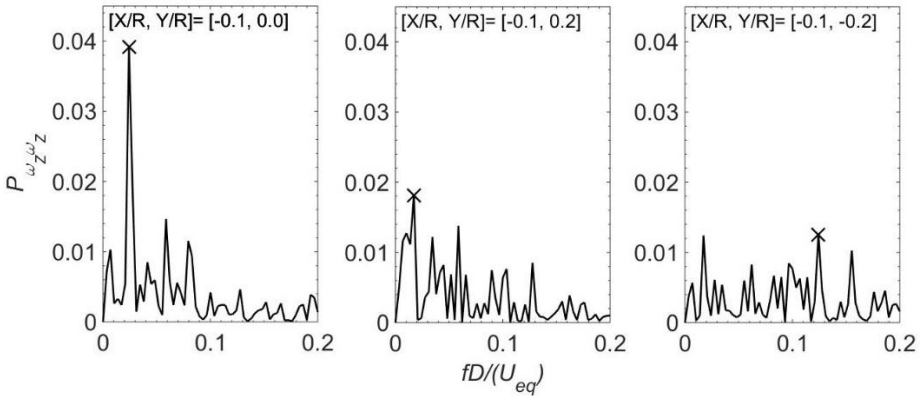

Fig. 8 Power spectrum analysis of Z-component vorticity at different locations in the wall parallel plane. $T_c = 27.3$.

Following the same method as performed in the wall-parallel plane, the spectral analysis of the X-component vorticity is conducted in the wall-normal plane (PIV arrangement 2) at $[Y/R,\ Z/R] = [-0.2, -0.9], [0, -0.9], [0.2, -0.9]$ (Fig.9), which are typical positions where ground vortices entering the propeller. An obvious peak value occurs at the frequency of blade passing, $fD/U_{eq} = 6.598$, for all the locations analysed. These peaks are ascribed to the effect of vorticity transportation, by which the vortices are stretched and tilted by the blade-induced velocities; therefore, the X-component vorticity varies according to the blade passing.

The dominant peak values are also observed at the frequency range of $fD/U_{eq} = O(10^{-2})\sim O(10^{-1})$ as shown in Fig. 9. The energetic frequencies involved in this range are close to that observed in the wall-parallel plane, which implies that they are due to the ground vortices originated from the ground and transported into the propeller plane. It is also noted that the dominant peak values occurs at relatively higher frequency compared with that in the wall-parallel plane, e.g. $fD/U_{eq} = 0.135$ at $[Y/R,\ Z/R] = [0.0, -0.9]$. This difference is ascribed to two possible reasons. Firstly, the damping effect in the viscous region near the ground changes the instability of the vortices. Secondly, it could also be due to the vortices originated from other regions of ground which is not covered by PIV arrangement 1 (this assumption is based on the computational fluid dynamics (CFD) simulations by the authors [19]. One instantaneous flow field from the simulations is shown in Fig. 10).

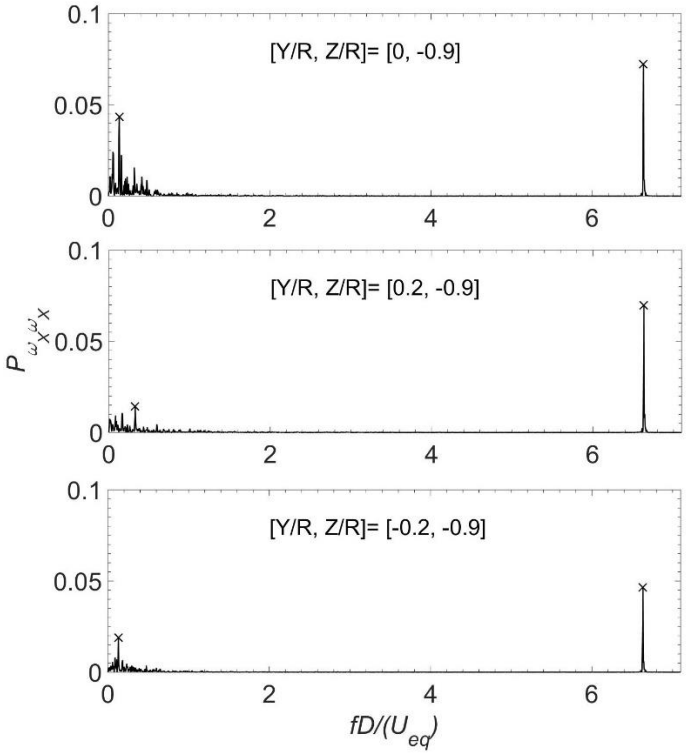

Fig. 9 Power spectrum analysis of X-component vorticity at different locations in the wall normal plane. $T_c = 27.3$.

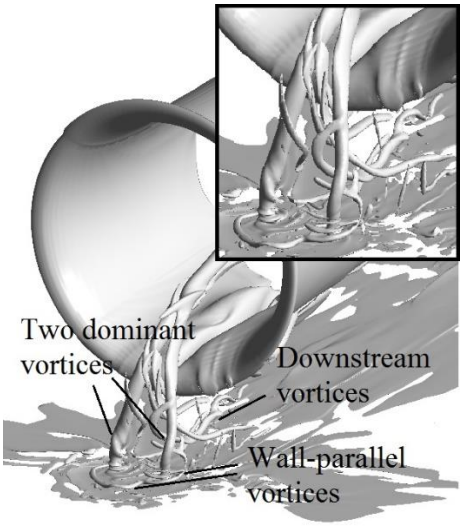

Fig. 10 Iso-surface of vorticity magnitude of one instantaneous flow field with two dominant vortices, $T_c = 27.3$. The data is from numerical simulations by actuator disk model [19].

The spectral analysis of ground vortices in the wall-parallel plane are compared at two different thrust coefficients, $T_c = 27.3$ and $T_c = 48.2$, as shown in the left hand side of Fig. 11. The energetic frequencies occur at the same range of the two thrust coefficients. However, as the thrust coefficient increases, the frequency of dominant peak value decreases. The spectral analysis in the wall-normal plane is performed at two different thrust coefficients as well, as shown in the right hand side of Fig. 11. One noticeable observation is that the frequency corresponding to blade passing increases as the thrust coefficient increases (the rotating speed of the propeller increases). The energetic frequencies at relatively low frequency are observed for both thrust coefficients and they are located in the same range; as the thrust coefficient increases, the most energetic frequency in the low frequency domain decreases, which is consistent with that observed in the wall parallel plane.

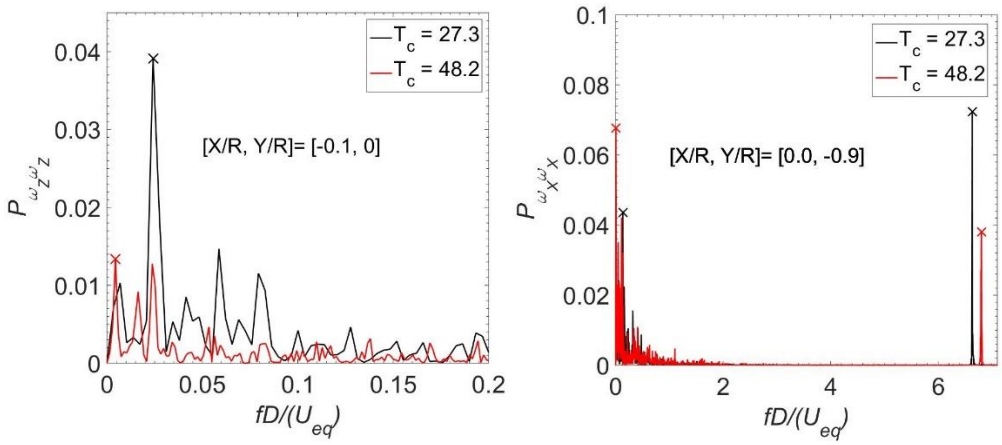

Fig. 11 Comparison of power spectra at different thrust coefficients. Left: Z-component vorticity in the wall-parallel plane; right: X-component vorticity in the wall-normal plane.

4.2.POD analysis

POD analysis in the flow fields near the wall

As already shown in section 4.1, even though the propeller is set at the same height ratio and thrust coefficient, multiple flow topologies are observed at different instants. It implies that the phenomenon of ground vortices is highly unsteady. In order to resolve this complex phenomenon, the coherent structures in the fluctuating flow is analysed with the help of Proper Orthogonal Decomposition (POD).

The POD analysis applied in the flow field of the wall parallel plane is introduced as follows. The turbulent kinetic energy fraction of each mode on the wall parallel plane is shown in the left hand side of Fig. 12. The cumulative energy of 88% is attained within the first 50 modes. It is found that 70% of the total amount of turbulent kinetic energy is captured by the first 10 modes, clearly indicating that the flow fluctuations are dominated by large scale coherent motions.

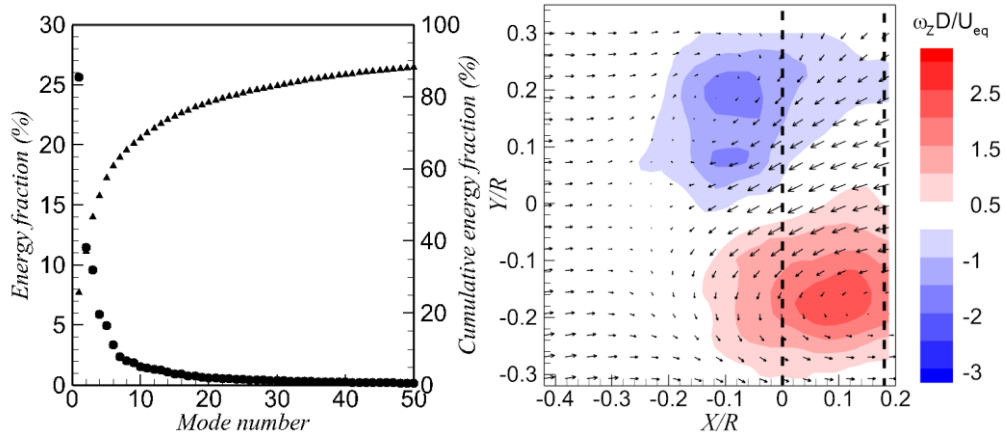

Fig. 12 Left: energy distribution of the flow modes; right: time averaged flow field in the wall parallel plane. $T_c = 27.3$.

The time averaged flow field is shown in the right hand side of Fig. 12. It features two vortices with opposite sign, but the magnitude of the vorticity is relatively low compared with the instantaneous flow fields, this is due to the meandering effect of the ground vortices.

The first mode represents 25.7% of the total turbulent kinetic energy, and its equivalent flow field is shown in the top left of Fig. 13. One dominant vortex can be observed below the propeller. The 2nd-4th modes represent 11.5%, 9.6%, and 5.9% of the turbulent kinetic energy, and feature a set of vortices. In order to investigate the flow structure corresponding to these modes, a conditional averaging of the flow fields is conducted (this method is reported in [20], and the idea of this method is to analyse the flow fields which have strong contributions to a specific mode).

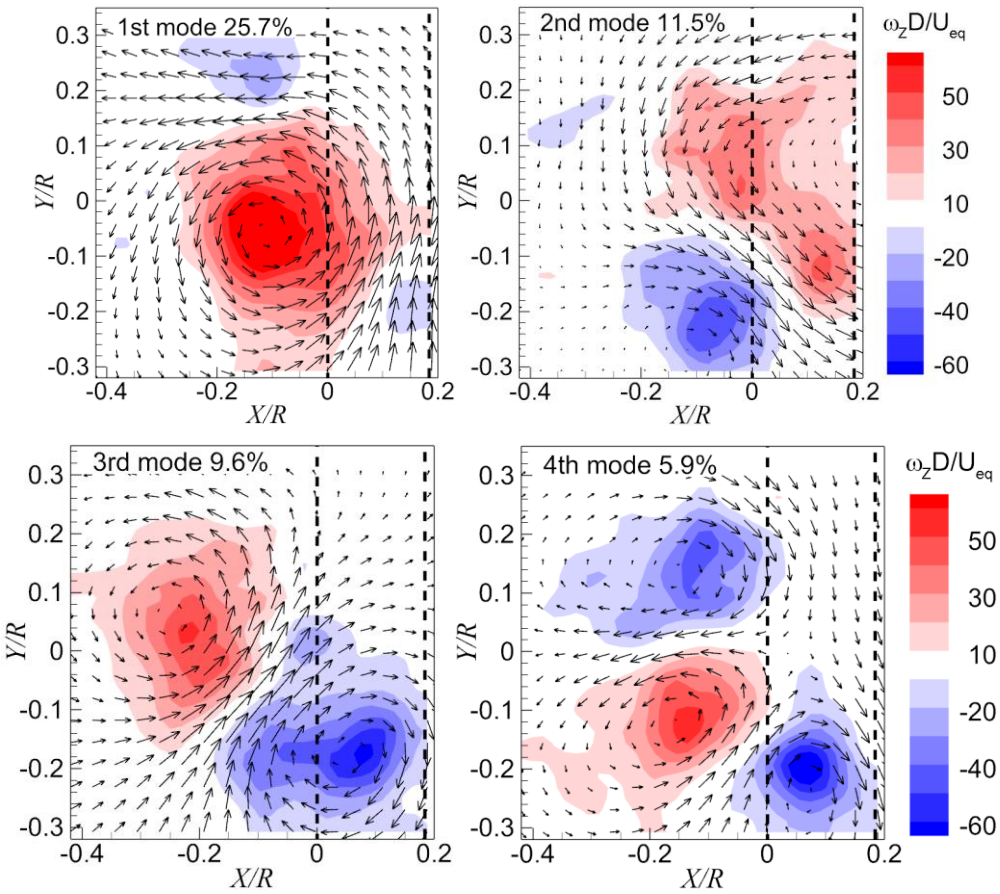

Fig. 13 The equivalent flow structures of the modes. Top left: first mode; top right: second mode; bottom left: third mode; bottom right: fourth mode. $T_c = 27.3$

For mode 1, two data subsets are selected according to the time coefficient of the first mode ($c_1 > 0.035$ and $c_1 < -0.035$, respectively). The value of this specific time coefficient is determined by its maximum magnitude and the number of samples for averaging (at least 20 samples in the current analysis). When $c_1 > 0.035$, there is one dominant vortex in the counter-clockwise direction in the conditional averaged result (shown in the top left of Fig. 14). Inversely, when $c_1 < -0.035$, there is one dominant vortex in clockwise direction (shown in the top right of Fig. 14). Therefore, the first mode is ascribed to the alternative sign of vortex in the flow field.

In the same way, the conditionally averaged results on the fourth mode are shown in the bottom row of Fig. 14. It is found that the fourth mode is mainly due to the change of the flow topology near the ground, specifically, the meandering of a pair of vortices near the ground. The same methodology can be applied to other modes, and they are not elaborated in detail here.

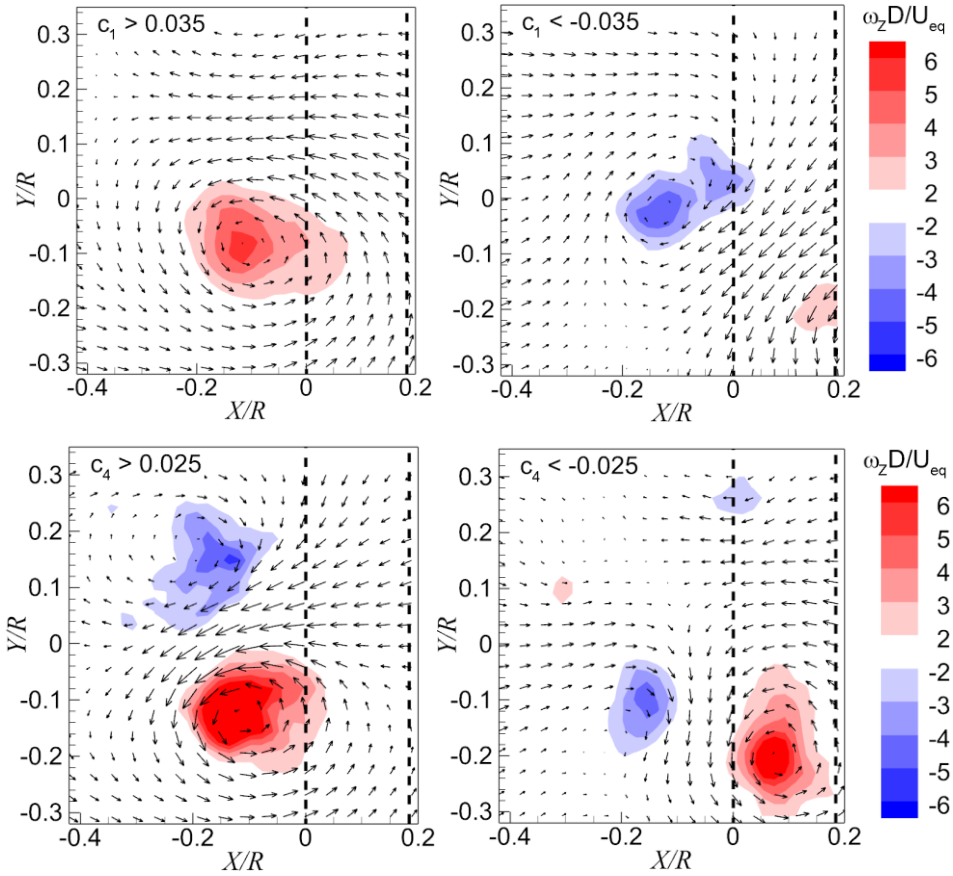

Fig. 14 Conditionally averaged flow field. Top left: $c_1 > 0.035$; top right: $c_1 < -0.035$; bottom left: $c_4 > 0.025$; bottom right: $c_4 < -0.025$. $T_c = 27.3$

At different thrust coefficients, the equivalent flow fields corresponding to the first mode in the wall parallel plane are shown in Fig. 15. The flow structure of the first mode at $T_c = 48.2$ is similar to that of $T_c = 27.3$, which features a dominant vortex upstream of the projection of the propeller on the wall; the fractions of turbulent kinetic energy are close as well. A difference is also noticed that the vortex moves upstream as the thrust coefficient increases. This is consistent with that observed in [6], which shows that as the thrust coefficient increases, the vortex meandering area on the ground moves upstream.

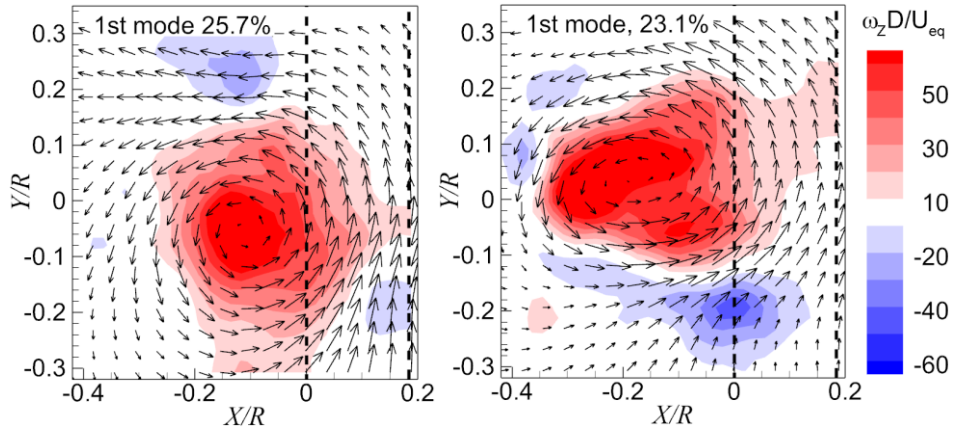

Fig. 15 Equivalent flow structures of the first mode in the wall-parallel plane. Left: $T_c = 27.3$; right: $T_c = 48.2$.

POD analysis in the flow fields in the plane upstream of the propeller

Following the same method, POD analysis is applied in the plane upstream of the propeller from PIV results. The fraction of turbulent kinetic energy for each mode and the cumulative energy of the modes are shown on the left hand side of Fig. 16. The cumulative energy of 73% is attained within the first 50 modes. It is found that 50% of the total amount of turbulent kinetic energy is captured

by the first 10 modes. The time averaged flow field of the plane upstream the propeller is shown on the right hand side of Fig. 16. The sign of X-component vorticity is opposite on the two sides of propeller, and the vorticity magnitude is relatively small compared with that in the instantaneous flow field, which is due to the vortex meandering as well.

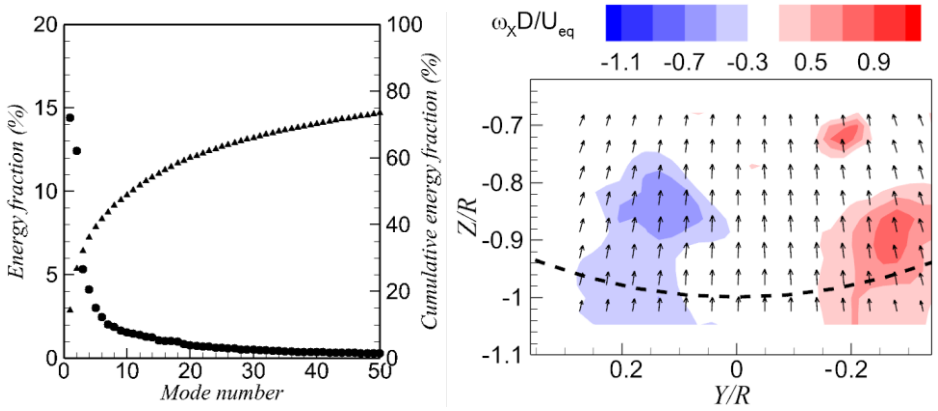

Fig. 16 Left: energy distribution of the flow modes; right: time averaged flow field in the wall normal plane. $T_c = 27.3$.

The first and second mode capture 14.4% and 12.4% of the total turbulent kinetic energy respectively. The equivalent flow structures of the first and the second modes are represented by contours of X-component velocity in Fig. 17. These two modes feature flow structures with contribution from X-component velocity. This X-component velocity is related to the propeller induced axial velocity upstream of the propeller.

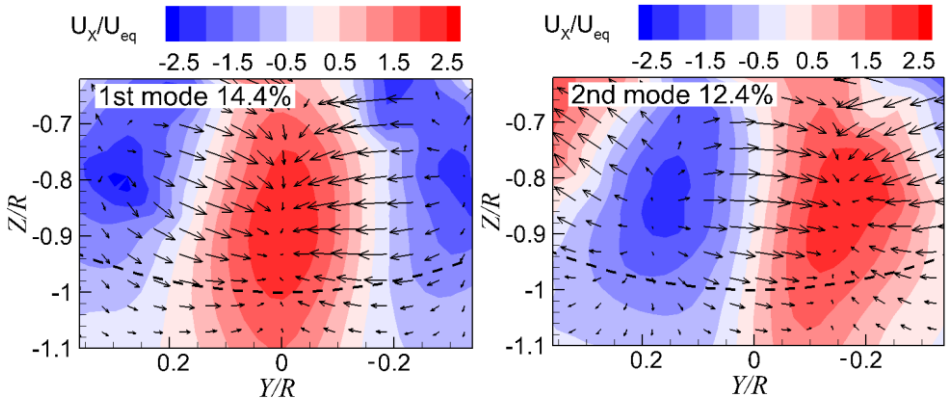

Fig. 17 Shape of the first and second POD modes in the plane upstream of the propeller color-coded by the axial velocity. T_c = 27.3.

To understand the behaviour of the first two modes, a joint statistical analysis is conducted on the time coefficients of the two modes, c_1 and c_2. As illustrated by the scatter plot in Fig. 18, a large correlation between the two modes is retrieved: whenever the first mode has high intensity, the second mode is weaker, and vice versa. The time coefficient plotted in the time domain corresponding to one revolution of the propeller is shown in the right hand side of Fig. 18. The wave lengths of the time coefficients of the two modes are close, and a 90° phase shift between these two modes is noticed.

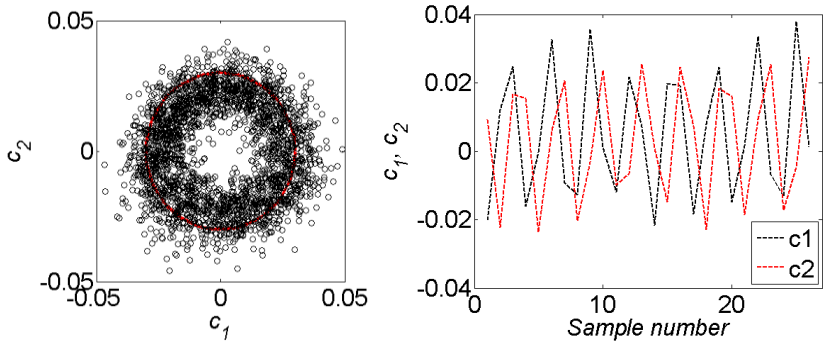

Fig. 18 Left: scatter plot of the time coefficient of the first and second mode; right: time coefficients of the modes (the first and second modes) in the time domain. T_c = 27.3.

The third mode exhibits one dominant vortex in the axial direction of the propeller, with the centre located around [*Y/R*, *Z/R*] = [0.08, -0.95], of which the vorticity contour is shown in the left hand side of Fig. 19. The third mode in the wall-normal plane is found to be consistent with the first mode in the wall-parallel plane, which implies that the dominant coherent flow structures formed near the ground retain after it leaves the ground. The fourth mode features a pair of vortices, which are located at the rim of the propeller projection, which is consistent with that observed in the second and the third modes in the wall-parallel plane.

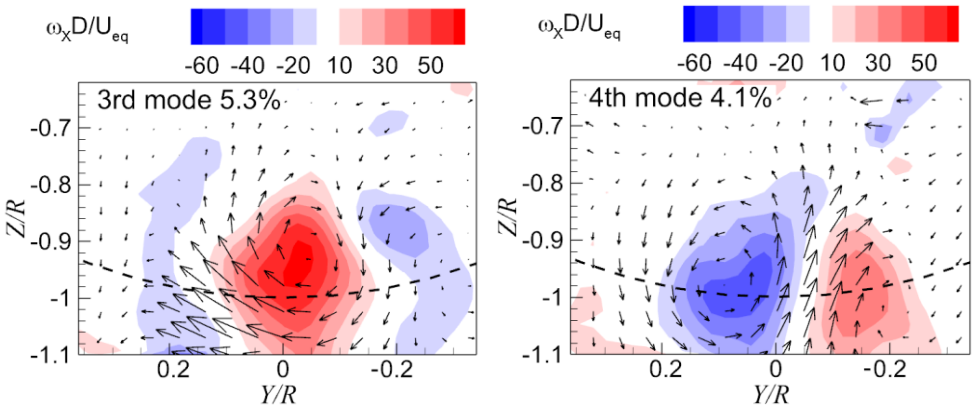

Fig. 19 Shape of the flow fields of the third mode (left) and fourth mode (right) in the plane upstream of the propeller. $T_c = 27.3$.

Furthermore, the third and fourth modes which are colour contoured by the axial velocity U_X are shown in Fig. 20. The contour of axial velocity is consistent with vortex structures as observed in Fig. 19. Because the vortex has an oblique angle when it enters the disk plane of the propeller, it has induced velocity which is in the axial direction of the propeller. For example, mode 4 which has two counter-rotating vortices can be depicted by the schematic as shown in Fig. 21. Their induced velocities in the axial direction (by the red circles as shown in Fig. 21) are consistent as that shown in the right hand side of Fig. 20.

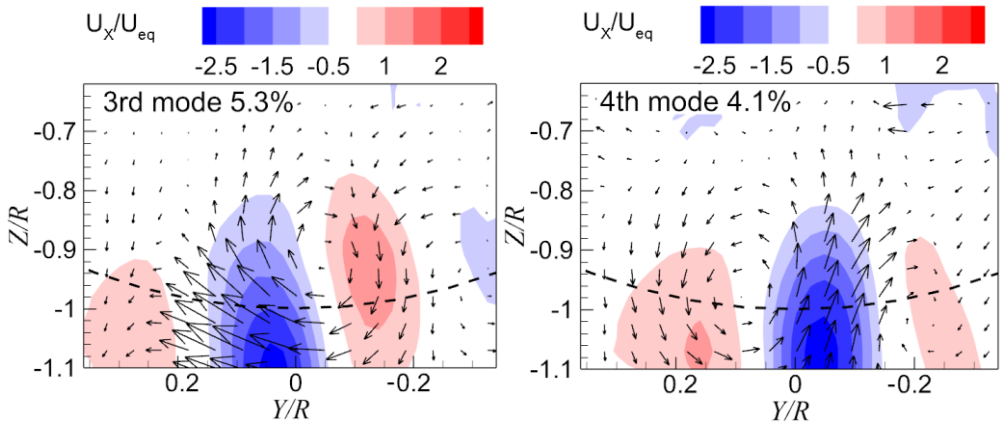

Fig. 20 Shape of the flow fields of the third mode (left) and fourth mode (right) in the plane upstream of the propeller, colour contoured by the out of plane component of velocity. $T_c = 27.3$.

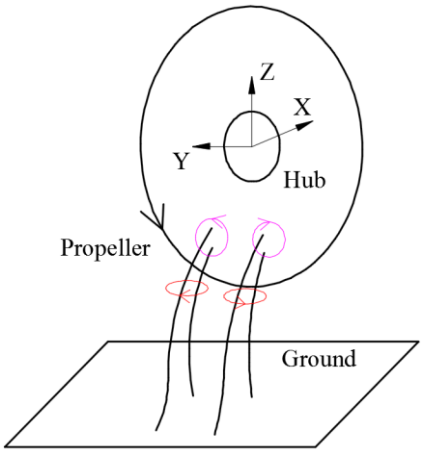

Fig. 21 Schematic of the vortices entering the propeller for mode 4.

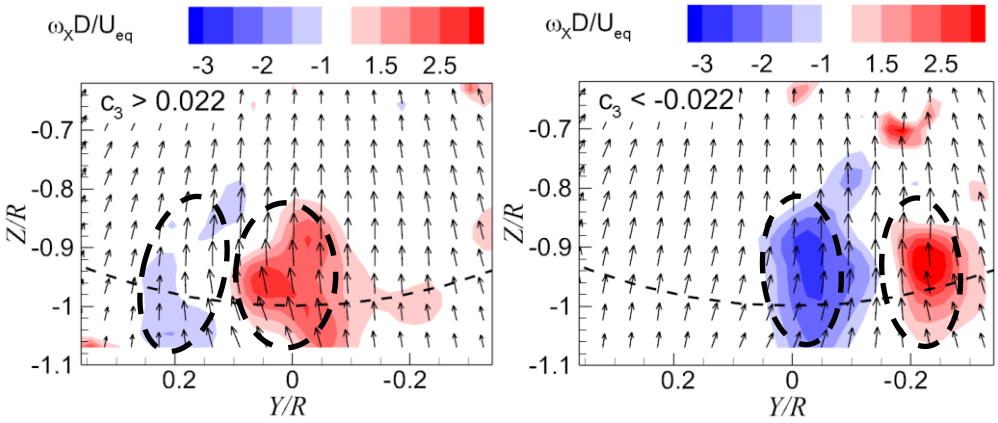

Fig. 22 Conditionally averaged flow fields for $c_3 > 0.022$ (left) and $c_3 < -0.022$ (right). $T_c = 27.3$.

Conditional averaging is performed on the selected instantaneous flow fields which contribute most to the third mode. The conditional averaged flow fields of $c_3 > 0.022$ is shown in the left hand side of Fig. 22, and that of $c_3 < -0.022$ is shown in the right hand side of Fig. 22. These two flow fields generally have two regions of concentrated vorticity (highlighted by the black-dashed circles) and their strength and position are different, which contribute to the flow structure of the third mode. The same analysis can be applied to the fourth mode and not elaborated here.

At two different thrust coefficients, i.e. $T_c = 27.3$ and $T_c = 48.2$, the flow structures of the third mode in the wall-normal plane are compared and shown in Fig. 23. The dominant flow structures at the two thrust coefficients are similar, which feature a dominant vortex located in the centre of the wall-normal plane. The main difference is the area where the dominant vortices located decreases which means the vortex meandering area decreases as the thrust coefficient increases.

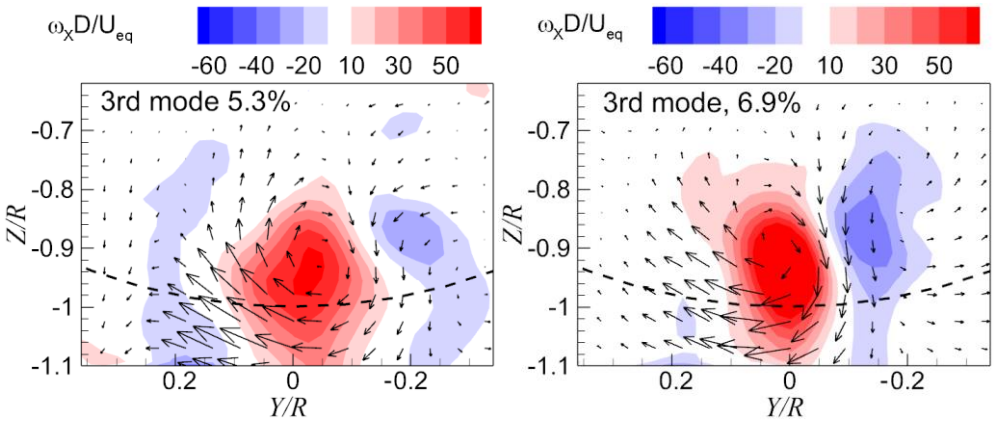

Fig. 23 Equivalent flow structure of the third mode in the wall-normal plane. Left: $T_c = 27.3$; right: $T_c = 48.2$.

Conclusions

Particle image velocimetry measurements have been conducted to investigate the flow fields generated by a propeller in ground proximity. At a low free-stream velocity, a highly loaded propeller in ground operation can induce vortical flow ascending from the ground to the propeller. The instantaneous flow fields feature several flow topologies: one dominant vortex, two dominant vortices and multiple vortices are observed in a sequence of instants, observed both in the wall-parallel plane and the wall-normal plane.

The spectral analysis on the vorticity performed in the plane in close proximity to the ground show energetic frequencies in the order of $fD/U_{eq} = O(10^{-2})\sim O(10^{-1})$, which is far below the blade passing frequency and implies that the flow near the ground has negligible influence from the blade passing. This relatively low frequencies are found to be consistent with that observed in the ground vortices induced by a suction tube model. In the wall-normal plane, the energetic frequencies not only occur at relatively low frequencies as observed near the ground, there is also a pulse at the blade passing frequency. This frequency is assumed to be due to the tilting and stretching of the vortices caused by the blade induced velocities. If we assume the vorticity in the vortex core stays constant by Kelvin's theorem, the vorticity in the area for analysis would change if the vortex is tilted or stretched. This results in the blade experiencing an intermittent inflow at high frequency as well. Furthermore, in the low frequency range ($fD/U_{eq} < O(10^{-1})$), the frequency of the vortices at the plane directly upstream of the propeller is also higher than that near the ground. This is probably ascribed to the viscous damping effect in the region near the ground; it could also be related to the vortices entering the propeller which are not captured in the measurement domain near the ground.

The flow involving ground vortices is analysed with the help of POD method to identify the coherent flow structures. The flow fields in the wall-parallel plane feature coherent structures with one vortex (first POD mode), two vortices (second and third mode), and multiple vortices (fourth mode). The first and second modes of the flow field upstream of the propeller are dominated by the blade passing and they have the same wave length and a 90^o phase angle shift; the modes due to ground vortices can be clearly observed in the third and higher modes. The third mode observed in the wall-normal plane is found to be consistent with that observed in the first mode of the wall-parallel plane; the fourth mode in the wall-normal plane is consistent with that of the 2nd-3rd mode of the wall parallel plane. This consistency means the coherent flow structures formed near the ground are transported to the inflow of the propeller without big changes.

Supplementary material

See supplementary materials for the video of unsteady flow measured in the wall-parallel and wall-normal planes respectively.

Acknowledgments

The authors would like to thank Teng Zhou for technical support, when he was a master student in TU Delft. We also would like to thank the Chinese Scholarship Council (CSC) for the funding.

Appendix: Boundary layer measurement of the ground table

The boundary layer above the ground table was measured without the existence of the propeller. The measurement of the flow near the ground was performed to help determine the position of the PIV measurement in the wall-parallel plane which is intended to be located inside the boundary layer and as close as possible to the ground. It also supports data for the velocity profile on the velocity inlet of the CFD simulation. The planar PIV measurement by a low frequency camera and a low frequency laser were utilized, and no detail of the experimental setup is elaborated here. The distribution of X component velocity is shown in Fig. 24.

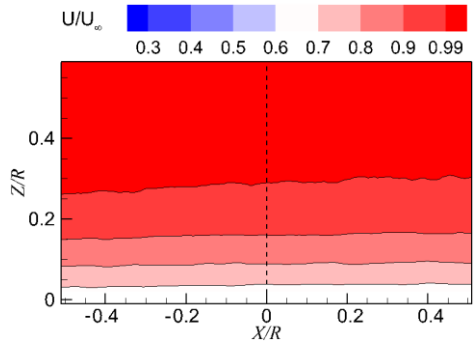

Fig. 24 Flow field near the ground wall without propeller. (Here, $Z = 0$ represents the plane of the ground, which has a shift of 1.46 R from the coordinates defined in Fig. 3. This new coordinate system is defined for clarity. The same for the following figures in this section)

The profile of the boundary layer at position $X/R = 0$, where it is aligned with the propeller's leading edge (although propeller does not exist in the flow during the boundary layer measurement), is plotted in the left hand side of Fig. 25. The boundary layer thickness is 0.45 R. The turbulence intensity of the flow near the wall, represented by u_X'/U_X (u_X' is the root mean square of velocity fluctuation), is plotted in the right hand side of Fig. 25. The maximum value of turbulence intensity is observed at the position close to the wall, which is around 4.3%. The maximum value of the turbulence intensity near the wall cannot be determined from our measurements. This position with maximum turbulence intensity is normally at the distance of order $O(10^{-3}\delta_{BL})$ for a turbulent boundary layer with zero pressure gradient along the wall as reported in [21], and it is not available in our measurements. The turbulence intensity outside the boundary layer in the free stream is approximately 0.5%.

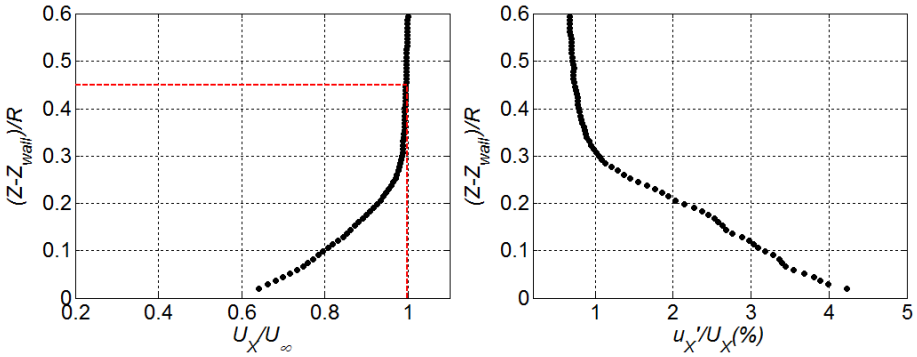

Fig. 25 Left: profile of the boundary layer at position $X/R = 0$; right: profile of the turbulent intensity at position $X/R = 0$;

References

[1] Rodert, L. A. and Garrett, F. B., "Ingestion of foreign objects into turbine engines by vortices," NACA TN-3330, Washington, D. C., 1955.

[2] Golesworthy, G. T., "Tests of a blow away jet debris guard applied to a supersonic turbojet intake," Royal aircraft establishment, C. P. No. 561, Bedford, 1961.

[3] De Siervi, F., Viguier, H. C., Greitzer, E. M., and Tan, C. S., "Mechanisms of inlet-vortex formation," J. Fluid Mech., Vol. 124, 1982, pp. 173-207.

[4] Murphy, J. P. and MacManus, D. G., "Inlet ground vortex aerodynamics under headwind conditions," Aerospace science and technology 15, 2011, pp. 207-215.

[5] Wang Z. and Gursul I., "Unsteady characteristics of inlet vortices," Exp Fluids, Vol. 53, 2012, pp. 1015-1032.

[6] Trapp, L. G., and Girardi, R., "Crosswind effects on engine inlets: The inlet vortex,", Journal of aircraft, Vol. 47, No. 2, 2010, pp. 577-590.

[7] Bissinger, N. C., and Braun, G. W., "On the inlet vortex system," NASA research grant NGL 43-001-086, Sep. 1974.
[8] Murphy, J. P., MacManus, D. G., and Sheaf, C. T., "Experimental investigation of intake ground vortices during takeoff," AIAA Journal, Vol. 48, No. 3, 2010, pp. 688-701.
[9] Lighthill, M. J., Introduction. Boundary layer theory. Laminar Boundary layers, ed. L. Rosenhead. 1963, Oxford University Press.

[10] Secareanu, A., and Moroianu, D., "Experimental and numerical study of ground vortex interaction in an air-Intake," 43rd AIAA Aerospace Sciences Meeting and Exhibit, 2005.

[11] Brix, S., Neuwerth, G. and Jacob, D., "The inlet-vortex system of jet engine operating near the ground," AIAA-2000-3998, 2000.

[12] Murphy, J. P. and MacManus, D. G., "Experimental investigation of intake ground vortices during takeoff," AIAA Journal, Vol. 48, No. 3, 2010, pp. 688-701.

[13] Campbell, J. F., and Chambers, J. R., "Patters in the sky: natural visualization of aircraft flow fields," NASA SP-514, 1994.

[14] Sciacchitano, A., Wieneke, B., and Scarano, F., "PIV uncertainty quantification by image matching," Meas. Sci. Technol. Vol. 24, 2013.

[15] Berkooz, G., Holmes, P., and Lumley, J., "The proper orthogonal decomposition in the analysis of turbulent flows," Annu. Rev. Fluid Mech., 1993, 25: 539-575.

[16] Sirovich, L., "Turbulence and the dynamics of coherent structures, Part I: Coherent structures," Quarterly of Applied Mathematics, Vol.45, No.3, pp. 561-571, 1987.

[17] Kourentis, L., and Konstantinidis, E., "Uncovering large-scale coherent structures in natural and forced turbulent wakes by combining PIV, POD, and FTLE," Exp Fluids, Vol. 52, pp. 749-763, 2012.

[18] Beresh, S. J., Henfling, J. F., "Meander of a fin trailing vortex and the origin of its turbulence," Exp Fluids, Vol. 49, pp. 599-611, 2010.

[19] Yang, Y., "Interaction between propeller and vortex: propeller self-induced vortices and externally induced vortex," PhD thesis, Delft University of Technology, 2016.

[20] Schrijer, F. F. J., Sciacchitano, A., and Scarano, F., *Spatio-temporal and modal analysis of unsteady* fluctuations *in a high-subsonic base flow.* Physics of Fluids, 2014. **26**(8): p. 086101.

[21] Klebanoff, P. S., "Characteristics of turbulence in a boundary layer with zero pressure gradient," NACA-TR-1247, 1955.